Journal of Sound and Vibration 433 (2018) 65–76

Contents lists available at ScienceDirect

Journal of Sound and Vibration

journal homepage: www.elsevier.com/locate/jsvi

The effect of flexural stiffness on the sound of a hanging filament: From a membrane to a rigid body

M. Weidenfeld, A. Manela *

Faculty of Aerospace Engineering, Technion - Israel Institute of Technology, Haifa 32000, Israel

ARTICLE INFO

Article history:
Received 16 December 2017
Revised 3 July 2018
Accepted 6 July 2018
Available online XXX
Handling Editor: D. Juve

Keywords:
Vibroacoustics
Hanging flag
Elasticity
Powell-Howe analogy

ABSTRACT

We consider the acoustic field of a thin flexible filament subject to uniform mean flow and a 'hanging chain' tension force parallel to its unperturbed state. The filament is actuated via harmonic heaving motion at its upstream edge with prescribed frequency and small amplitude. To investigate the effect of filament flexural rigidity, we analyze the system acoustic radiation in the entire range of body structural stiffnesses. Assuming two-dimensional high Reynolds and low Mach number flow, we apply a near-field description based on potential thin airfoil theory. The near-field model is then used to formulate the source term in the Powell-Howe acoustic analogy. The far field sound is calculated applying a compact Green's function approach, yielding the leading order acoustic dipole field. In the limit of small flexural stiffness, we find that the acoustic field of a highly-elastic filament converges to the far field of a hanging membrane, dominated by the wake dipole sound. The wake sound component also dominates the system radiation in the limit of small actuation frequencies, where the filament deflects as a rigid body regardless of its structural stiffness. Sufficient increase in heaving frequency intensifies the relative contribution of filament motion dipole, resulting in significant differences between systems with different rigidities. Reflecting the impact of filament elasticity, these differences manifest the system's natural frequency response, leading to increased levels of sound for actuations at the system's eigenstates. In cases where the trailing edge wake and motion dipoles acquire similar amplitudes and opposite phases, significant sound reduction is found.

1. Introduction

The acoustics of fluid-structure interactions, coupling the near-field fluid-structure dynamics of a body with its far acoustic signature, is a topic of extensive studies owing to its relevance in a large variety of engineering and natural applications [1]. These include, among others, the modeling of palatal snoring and its control [2]; the production of "insect songs" and its social role in various species of flies [3,4]; the analysis and biomimicry of silent flight in birds [5,6]; and the study of turbomachinery aerodynamic noise, a key component in aviation sound pollution [7,8]. All of these have motivated ongoing progress in the field of vibroacoustics, where the far-field noise generated by mechanically- and flow-induced body motions is considered. Existing studies are typically based on an acoustic analogy technique, where the near-field calculation serves as an effective source term, and an appropriate analogy is applied to predict the far acoustic pressure. Such a scheme appears superior over a direct numerical calculation of the entire flow field, as the far radiated signal turns prohibitively small (and, at some point, of the order

* Corresponding author.
E-mail address: amanela@technion.ac.il (A. Manela).

https://doi.org/10.1016/j.jsv.2018.07.014
0022-460X/

of the numerical error of the pertinent computational solver) far enough from the source. A first step into application of this approach is therefore the determination of the near-field fluid-structure dynamics of the configuration of interest.

Focusing on the near-field interaction between elastic bodies and a surrounding flow field, a large number of recent works have considered the model "flapping flag" problem, where a thin filament is immersed in uniform flow and exhibits either flow-induced or mechanically-imposed motions [9,10]. The associated setup has been shown relevant in a variety of applications, including the development of energy harvesting methodologies [11] and the optimization of propulsion efficiencies in single- and multi-body environments [12,13]. In the context of aeroacoustics, the flag model has been applied to evaluate the aerodynamic sound radiated during flapping flight [14,15].

In common to the above near- and far-field investigations, structural elasticity, modeled as a flexural stiffness term in the filament equation of motion, has a key effect in determining the system dynamics, in terms of both body motions and associated body-flow interactions. Yet, a detailed investigation of the gradual impact of rigidity on the system aeroacoustic properties is lacking. Such a study should rationalize the effect of body flexibility, at different magnitudes, on the system acoustic signature. In particular, the results may indicate on optimal conditions where the noise may be minimized, as a possible means for sound monitoring.

The present work aims at studying the effect of body flexural stiffness, varying between vanishingly small (membrane) and exceedingly large (rigid body) values, on its far-field signature. In the small-stiffness limit, large body deformations develop unless the dampening effect of filament tension is taken into account. Indeed, inasmuch as bending rigidity exists for all elastic structures, tension forces always prevail to some extent. Such forces may originate from either structure-induced effects, viscous boundary layer loading, or other forms of external forcing acting parallel to the unperturbed body state. In the small-amplitude motion regime, it was shown that the effect of structure-induced tension is of higher order and may be neglected [16]. Additionally, the relatively small magnitude of drag-induced tension at high Reynolds numbers makes its impact relatively minor [17]. Small-amplitude motion at small stiffness rates may consequently occur in the presence of stronger tension forces.

To consider the effect of externally-induced tension at low-rigidity conditions, several works have examined the "hanging-filament" setup. Among others, Datta and Gottenberg [18] have studied the free vibrations developed in an infinitely long elastic strip hanging vertically in a downward stream, by using a simplified model for the fluid pressure loading. Lemaitre et al. [19] have applied a similar theoretical approach to analyze the flutter instability of a long ribbon hanging in axial flow, and validated their results experimentally. Several workers have later on suggested the hanging-filament setup as an efficient means for energy harvesting purposes [20–22]. The specific efficiency of a piezoelectric membrane hanging in axial flow was analyzed in detail [22,23]. In a recent contribution, the singular limit of small stiffness ratio has been examined for a "hanging flag" setup [24]. The convergence of a beam-type (having arbitrarily small rigidity) to a membrane-type description has been discussed, and the inevitable effect of body stiffness on the structure dynamics near its end points has been analyzed.

In view of the above investigations on the effect of small stiffness ratio on the motion of hanging elastic bodies, a study on their far-field properties is of interest. Apart from the fundamental significance of such a study, it may be useful for analyzing the acoustic field of the associated energy harvesting systems, generally known as a major concern in the design of industrial wind farms [25]. In common with Ref. [24], we consider a "hanging flag" setup. This permits investigation of the system far field sound in the entire range of body flexural rigidities, while maintaining the assumption of small-amplitude structural deflections even in the limit of vanishing rigidity. The two-dimensional configuration consists of a thin filament subject to leading-edge heaving actuation and a gravity force acting in parallel to the structure unperturbed state. Small body deflections are considered, so that the filament equation of motion may be linearized about its non-deflected state. Low-Mach and high-Reynolds number flow conditions are assumed, enabling application of a compact-body acoustic analogy for the prediction of the far field sound. In the subsequent section, the near- and far-field problems are formulated. Our results, analyzing the system response to harmonic actuation, are presented in Section 3, and concluding comments are given in Section 4.

2. Problem formulation

Schematic of the problem is shown in Fig. 1. Consider a two-dimensional setup of a thin elastic filament of chord $2a$ immersed in uniform flow of speed U in the x_1-direction. The filament is subject to a 'hanging-chain' gravity-induced tensile force [26]

$$T(x_1) = \rho_s g(a - x_1), \tag{1}$$

where ρ_s marks the structure mass per unit area, and g is the constant of gravitational acceleration. Mechanical loading is applied to the body, in the form of harmonic leading-edge heaving actuation

$$\xi(-a, t) = \overline{\varepsilon}_h a \sin\left(\omega_h t\right). \tag{2}$$

In Eq. (2), $\xi(x_1, t)$ denotes the filament displacement in the x_2-direction, $\overline{\varepsilon}_h \ll 1$ is the scaled heaving amplitude (with an overbar marking a non-dimensional quantity), and ω_h is the prescribed heaving frequency. In what follows, we investigate the acoustic far field generated by the fluid-structure interaction of the vibrating body with the flow. In a practical setup, the physical apparatus driving the filament actuation (2) should also contribute to the near- and far-field behaviors of the system. While such consideration is particularly important when conducting experimental measurements (see, e.g. Purohit et al. [27]), we regard this mechanism as "ideal" hereafter, so that its impact on the filament signature is not analyzed. High Reynolds and low Mach number conditions are assumed, thus considering the near field to be inviscid and incompressible. Compressibility effects are

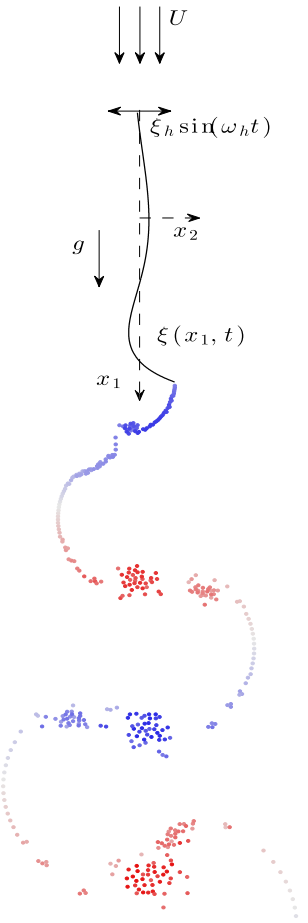

Fig. 1. Schematic of the hanging-filament setup.

taken into account when analyzing the far-field sound, focusing on the low-frequency limit of an acoustically compact configuration.

2.1. Recapitulation of the near-field model

We make use of the near-field description formulated in Ref. [24] to examine the effect of body flexural rigidity on the system acoustic signature in the entire range of stiffness values. For later convenience, the near-field model is recapitulated.

Assuming small-amplitude motion, the filament displacement $\xi(x_1, t)$ is governed by the linearized equation of motion

$$\rho_s \frac{\partial^2 \xi}{\partial t^2} + EI \frac{\partial^4 \xi}{\partial x_1^4} - \rho_s g \frac{\partial}{\partial x_1} \left((a - x_1) \frac{\partial \xi}{\partial x_1} \right) = \Delta p(x_1, t), \tag{3}$$

balancing structural inertia, bending stiffness, tensile force, and fluid loading terms. On the right-hand side, $\Delta p = p_- - p_+$ marks fluid pressure jump between the filament lower (p_-) and upper (p_+) surfaces. Applying thin-airfoil theory, $\Delta p(x_1, t)$ is determined by the unsteady Bernoulli's equation,

$$\Delta p(x_1, t) = \rho_0 U \gamma \left(x_1, t \right) + \rho_0 \frac{\partial}{\partial t} \int_{-a}^{x_1} \gamma \left(s, t \right) \mathrm{d}s, \tag{4}$$

where ρ_0 denotes the fluid mean density, and $\gamma \left(x_1, t \right)$ marks the distribution of filament circulation per unit length along the chord. Eqs. (3) and (4) are supplemented by the unsteady Kutta condition,

$$\gamma(a, t) = 0, \tag{5}$$

imposing regularization of the flow at the structure downstream end, together with a set of actuated-free end conditions (see Eq. (2)),

$$\xi(-a,t)=\overline{\varepsilon}_h a\sin(\omega_h t)\,,\ \left(\frac{\partial\xi}{\partial x_1}\right)_{(-a,t)}=0\,,\ \left(\frac{\partial^2\xi}{\partial x_1^2}\right)_{(a,t)}=0\,,\ \left(\frac{\partial^3\xi}{\partial x_1^3}\right)_{(a,t)}=0. \tag{6}$$

Necessitated by the unsteady flow conditions and the Kelvin theorem, continuous vortex shedding occurs at the structure surface. At the small angles of attack assumed, the flow at the filament upstream end and along its chord is regarded attached, and release of vorticity is allowed only at the structure downstream edge. To describe the time evolution of filament wake, we make use of a discrete-vortex model [24,28], where, at each time step, a concentrated line vortex is released to the flow, with its strength Γ_k fixed by the Kelvin theorem and the instantaneous time change in filament circulation (see Fig. 1). At each time step Δt, the nascent point vortex is placed at a distance $U\Delta t$ in the mean-flow direction from the instantaneous position of the trailing edge. Once released, the trajectory of each wake vortex follows from a potential-flow calculation, as formulated below (see Eq. (10)). Applying complex notation and denoting the conjugate velocity of the potential flow-field by $W(z)$, the impermeability condition takes the form

$$\frac{\partial\xi}{\partial t}+U\frac{\partial\xi}{\partial x_1}=-\,\mathrm{Im}\{W(z)|_{-a\le x_1\le a}\}, \tag{7}$$

where

$$W(z)=U-\frac{i}{2\pi}\left(\sum_{k=1}^{N}\frac{\Gamma_k}{z-z_{\Gamma_k}}+\int_{-a}^{a}\frac{\gamma\,(s,t)\,\mathrm{d}s}{z-s}\right). \tag{8}$$

At the filament surface

$$W(z)|_{-a\le x_1\le a}=U-\frac{i}{2\pi}\left(\sum_{k=1}^{N}\frac{\Gamma_k}{x_1-z_{\Gamma_k}}+\fint_{-a}^{a}\frac{\gamma\,(s,t)\,\mathrm{d}s}{x_1-s}\right), \tag{9}$$

where the barred integral sign denotes a Cauchy principal value integral. In Eqs. (7)–(9), $z=x_1+\mathrm{i}x_2$ marks the complex representation of a point in the plane of motion, and $z_{\Gamma_k}=z_{\Gamma_k}(t)$ denotes the instantaneous location of the k-th trailing edge vortex. Applying potential-flow theory, the motion of each of the wake vortices is governed by

$$\frac{\mathrm{d}z_{\Gamma_k}}{\mathrm{d}t}=W^*_{\Gamma_k}\quad(k=1,2,\ldots,N), \tag{10}$$

where $W^*_{\Gamma_k}$ marks the complex conjugate of the conjugate velocity induced at the instantaneous location of the k-th wake vortex after removing its self-singularity,

$$W_{\Gamma_k}=U-\frac{i}{2\pi}\left(\sum_{\substack{m=1\\ m\neq k}}^{N}\frac{\Gamma_m}{z_{\Gamma_k}-z_{\Gamma_m}}+\int_{-a}^{a}\frac{\gamma\,(x_1,t)\,dx_1}{z_{\Gamma_k}-x_1}\right). \tag{11}$$

The total system circulation is conserved by applying the Kelvin's theorem,

$$\Gamma_N=-\left(\sum_{k=1}^{N-1}\Gamma_k+\int_{-a}^{a}\gamma(x_1,t)\mathrm{d}x_1\right), \tag{12}$$

which fixes the strength of the nascent vortex Γ_N. We formulate an initial-value problem, and assume that release of the first trailing edge vortex occurs at $t=0$, where the filament initial deflection vanishes. At the same time, leading-edge actuation commences, and the system evolution follows through its final periodic state. Details regarding the numerical procedure are given in Section 2.3.

2.2. Acoustic-field description

We now turn to analyze the far-field radiation of the system, where the near-field description serves as an effective "source term". Considering the present low-Mach and high-Reynolds number setup, the acoustic field is governed by the equation of vortex sound [29],

$$\left(\frac{1}{c_0^2}\frac{\partial^2}{\partial t^2}-\nabla^2\right)B=\mathrm{div}\,(\boldsymbol{\Omega}\times\mathbf{v})\,, \tag{13}$$

where c_0 marks the mean speed of sound, $B = \int \mathrm{d}p/\rho + v^2/2$ denotes fluid total enthalpy for homentropic flow (with p, ρ and v marking the fluid acoustic pressure, density and velocity magnitude, respectively), $\mathbf{v}$ is the fluid velocity, and $\mathbf{\Omega}$ is the vorticity vector. The latter is composed of the discrete contributions of wake vortices,

$$\mathbf{\Omega} = \sum_{k=1}^{N} \mathbf{\Omega}_{\Gamma_k} = \hat{\mathbf{x}}_3 \sum_{k=1}^{N} \Gamma_k \delta\left(\mathbf{x} - \mathbf{x}_{\mathbf{\Gamma_k}(t)}\right), \tag{14}$$

and δ denotes the Dirac delta function. In the far-field ($|\mathbf{x}| \to \infty$)

$$B(\mathbf{x}, t) \approx p(\mathbf{x}, t)/\rho_0, \tag{15}$$

and we focus on evaluating the distant $|\mathbf{x}| \to \infty$ approximation for $p(\mathbf{x}, t)$. Applying a Green's function approach, we formulate the problem satisfied by the Green's function G [29],

$$\left(\frac{1}{c_0^2}\frac{\partial^2}{\partial t^2} - \nabla^2\right) G\left(\mathbf{x}, \mathbf{y} | t - t_0\right) = \delta(\mathbf{x} - \mathbf{y})\,\delta\left(t - t_0\right), \tag{16}$$

where $\mathbf{x}$ and $\mathbf{y}$ denote observer and point-source vector locations, respectively, and t_0 marks the time instant of source action. Imposing a Neumann-type boundary condition of a vanishing normal derivative of G over the filament surface, $(\partial G/\partial y_n)_{\text{filament}} = 0$, and making use of Eq. (15), we arrive at an expression for the far-field acoustic pressure,

$$p(\mathbf{x}, t) \approx -\int_{-\infty}^{\infty} \mathrm{d}\tau \int_{-\infty}^{\infty} \rho_0 (\mathbf{\Omega} \times \mathbf{v}) \nabla G \mathrm{d}^3\mathbf{y} + \int_{-\infty}^{\infty} \mathrm{d}\tau \oint_{\text{filament}} \rho_0 G \frac{\partial v_n}{\partial \tau} \mathrm{d}S(\mathbf{y}), \quad |\mathbf{x}| \to \infty, \tag{17}$$

where v_n marks the component of fluid velocity normal to the filament.

We consider a case where the airfoil is acoustically compact, in which the characteristic size of the source (being the filament length) is much smaller than the acoustic wavelength. Assuming an acoustic wave with frequency ω_0 and associated wavelength $\lambda_0 = 2\pi c_0/\omega_0$, this is equivalent to requiring that $a/\lambda_0 = M(\omega_0 a/2\pi U) \ll 1$, where $M = U/c_0$ is the mean-flow Mach number. At the low-Mach flow conditions considered, source compactness is therefore ensured when sufficiently low wave frequencies (in convective U/a units) are taken. The two-dimensional compact Green's function applied is [29].

$$G(\mathbf{x}, \mathbf{y}, t - \tau) \approx \frac{\mathbf{x} \cdot \mathbf{Y}}{2\pi\sqrt{2c_0}|\mathbf{x}|^{3/2}} \frac{\partial}{\partial t}\left\{\frac{\mathrm{H}(t_r - \tau)}{\sqrt{t_r - \tau}}\right\}, \quad |\mathbf{x}| \to \infty, \tag{18}$$

where $t_r = t - |\mathbf{x}|/c_0$ denotes the acoustic retarded time, H is the unit step function, and $\mathbf{Y}(\mathbf{y})$ marks the *Kirchhoff vector*, which components express flow potentials of unit flow over a thin flat airfoil in the y_1- and y_2-directions,

$$\mathbf{Y}(\mathbf{y}) = \left(y_1, \mathrm{Re}\left\{-i\sqrt{\left(y_1 + iy_2\right)^2 - a^2}\right\}\right), \tag{19}$$

respectively.

Taking account of the linear property of the far-field problem and the above form of the acoustic Green's function, the acoustic pressure may be expressed as a superposition of "filament motion" and "wake" contributions,

$$p(\mathbf{x}, t) = p_{\xi}(\mathbf{x}, t) + p_w(\mathbf{x}, t), \tag{20}$$

where

$$p_{\xi}(\mathbf{x}, t) = \rho_0 \int_{-\infty}^{\infty} \oint_{\text{filament}} G(\mathbf{x}, \mathbf{y}, t - \tau) \frac{\partial^2 \xi}{\partial \tau^2} \mathrm{d}S(\mathbf{y}) \mathrm{d}\tau \tag{21}$$

and

$$p_w(\mathbf{x}, t) = -\rho_0 \sum_{k=1}^{N} \int_{-\infty}^{\infty} \int_{\mathcal{V}} \left(\mathbf{\Omega}_{\Gamma_k} \times \mathbf{V}_{\Gamma_k}\right) \cdot \frac{\partial G}{\partial \mathbf{y}}(\mathbf{x}, \mathbf{y}, t - \tau)\, \mathrm{d}S(\mathbf{y}) \mathrm{d}\tau. \tag{22}$$

In Eqs. (21) and (22), $\mathcal{V}$ denotes the fluid volume occupying all vortices, and $\mathbf{V}_{\mathbf{\Gamma_k}}$ marks the velocity vector of the kth wake vortex. Substituting Eqs. (14), (18), and (19) into Eqs. (21) and (22) yields

$$p_{\xi}(\mathbf{x}, t) = \frac{\rho_0 \cos\theta}{2\pi\sqrt{2c_0\,|\mathbf{x}|}} \frac{\partial}{\partial t} \int_{-\infty}^{t_r} \frac{\mathrm{d}\tau}{\sqrt{t_r - \tau}} \int_{-a}^{a} \sqrt{a^2 - y_1^2}\, \frac{\partial^2 \xi}{\partial \tau^2}(y_1, \tau) \mathrm{d}y_1 \tag{23}$$

and

$$p_w(\mathbf{x}, t) = \sum_{k=1}^{N} \left(\frac{\rho_0 \Gamma_k \sin\theta}{2\pi\sqrt{2c_0\,|\mathbf{x}|}} \frac{\partial}{\partial t} \int_{-\infty}^{t_r} \frac{V_{\Gamma_k}^{(2)}(\tau)\mathrm{d}\tau}{\sqrt{t_r - \tau}} - \frac{\rho_0 \Gamma_k \cos\theta}{2\pi\sqrt{2c_0\,|\mathbf{x}|}} \frac{\partial}{\partial t} \int_{-\infty}^{t_r} \frac{\mathrm{d}\tau}{\sqrt{t_r - \tau}} \left(V_{\Gamma_k}^{(1)}(\tau) \frac{\partial Y_2}{\partial y_2} - V_{\Gamma_k}^{(2)}(\tau) \frac{\partial Y_2}{\partial y_1} \right)_{\mathbf{x}_{\mathbf{\Gamma_k}}(\tau)} \right). \tag{24}$$

In Eq. (24), $V_{\Gamma_k}^{(j)}$ marks the velocity component of the kth wake vortex in the x_j-direction. The angle θ indicates the far-field observer's directivity, and is measured relative to the x_2-axis in the clockwise direction. The $\cos\theta = x_2/|x|$ and $\sin\theta = x_1/|x|$ terms in (23) and (24) therefore correspond to "lift" and "suction" dipole-type radiations. The wake vortex sound includes both lift and suction dipoles, reflecting vortices displacements in the x_1 and x_2 directions, respectively. The filament motion dipole contains only a lift component, and therefore vanishes along the mean-flow ($\theta = \pi/2$) direction. The suction dipole ($\propto \sin\theta$) contained in the wake sound expression reflects the effect of leading edge suction force and consequent contribution to the release of trailing edge vortices.

Calculation of the far-field pressure components is carried out numerically, based on the near-field solution described in Section 2.1. In the limit case of a rigid filament, p_ξ may be expressed in a closed form by substituting

$$\xi(x_1,t) = \xi_{\text{rigid}}(x_1,t) = \overline{\varepsilon}_h a \sin\left(\omega_h t\right) \tag{25}$$

into Eq. (23) and taking the long-time limit. This yields

$$p_{\xi_{\text{rigid}}}(\mathbf{x},t) \approx \frac{\sqrt{2\pi}\rho_0 a^3 \cos\theta}{4\sqrt{c_0|\mathbf{x}|}} \overline{\varepsilon}_h \omega_h^{5/2} \cos\left(\omega_h t_r - \pi/4\right), \quad t_r \gg \omega_h^{-1}, \tag{26}$$

indicating an $O(\omega_h^{5/2})$ power increase in filament motion sound with increasing pitching frequency [30].

2.3. Scaling and numerical analysis

To obtain a numerical solution, the dimensional problem formulated in Sections 2.1 and 2.2 is non-dimensionalized using the aerodynamic scales a, U, a/U, $\rho_0 U^2$ and $2\pi a U$ for the length, velocity, time, pressure and vortices circulations, respectively. Omitting presentation of the full non-dimensional problem for brevity, the scaled form of the filament equation of motion (3) is

$$\overline{\mu}\,\overline{\alpha}\frac{\partial^2\overline{\xi}}{\partial\overline{t}^2} + \overline{R}\frac{\partial^4\overline{\xi}}{\partial\overline{x}_1^4} - \frac{\partial}{\partial\overline{x}_1}\left(\left(1-\overline{x}_1\right)\frac{\partial\overline{\xi}}{\partial\overline{x}_1}\right) = \overline{\alpha}\Delta\overline{p}, \tag{27}$$

accompanied by the scaled form of the boundary conditions (6),

$$\overline{\xi}(-1,\overline{t}) = \overline{\varepsilon}_h \sin(\overline{\omega}_h\overline{t}), \left(\frac{\partial\overline{\xi}}{\partial\overline{x}_1}\right)_{(-1,\overline{t})} = 0, \left(\frac{\partial^2\overline{\xi}}{\partial\overline{x}_1^2}\right)_{(1,\overline{t})} = 0, \left(\frac{\partial^3\overline{\xi}}{\partial\overline{x}_1^3}\right)_{(1,\overline{t})} = 0. \tag{28}$$

The near-field problem is then governed by the non-dimensional parameters

$$\overline{\mu} = \frac{\rho_s}{\rho_0 a}, \quad \overline{\alpha} = \frac{\rho_0 U^2}{\rho_s g}, \quad \overline{R} = \frac{EI}{\rho_s g a^3}, \quad \overline{\varepsilon}_h \quad \text{and} \quad \overline{\omega}_h = \frac{a}{U}\omega_h, \tag{29}$$

denoting the filament to fluid mass ratio, fluid to filament gravity-driven inertia, normalized filament rigidity, and scaled heaving amplitude and frequency, respectively. To illustrate our findings, we consider a case where small-amplitude heaving is applied, $\overline{\varepsilon}_h = 0.01$, and take a fixed choice of $\overline{\mu} = 5$ and $\overline{\alpha} = 0.2$. We then investigate the impact of the body stiffness parameter $\overline{R}$, and the heaving actuation frequency $\overline{\omega}_h$, on the system acoustic radiation. By varying $\overline{R}$ between the values $\overline{R} \ll 1$ and $\overline{R} \gg 1$, we aim at characterizing the differences between the acoustic properties of a highly elastic and a nearly rigid body. The limit cases of a membrane ($\overline{R} = 0$) and a rigid filament ($\overline{R} \to \infty$) are taken as reference setups, and the above-mentioned choice of $\overline{\mu} = 5$ and $\overline{\alpha} = 0.2$ ensures that no large-amplitude filament displacements occur. Our numerical calculations indicate that no qualitative differences are observed when choosing other subcritical $(\overline{\mu},\overline{\alpha})$ combinations.

Applying the same non-dimensionalization to the acoustic problem, the normalized form of the acoustic pressure becomes

$$\overline{p}(\overline{\mathbf{x}},\overline{t}) = \sqrt{\frac{M}{8|\overline{\mathbf{x}}|}}\Pi_{\text{tot}}(\overline{t}_r) = \sqrt{\frac{M}{8|\overline{\mathbf{x}}|}}\left(\Pi_{\xi}(\overline{t}_r) + \Pi_w(\overline{t}_r)\right), \tag{30}$$

where

$$\Pi_{\xi}(\overline{t}_r) = \frac{2}{\pi}\cos\theta\frac{\partial}{\partial\overline{t}}\int_{-\infty}^{\overline{t}_r}\frac{\mathrm{d}\tau}{\sqrt{\overline{t}_r-\tau}}\int_{-1}^{1}\sqrt{1-y_1^2}\,\frac{\partial^2\overline{\xi}}{\partial\tau^2}(y_1,\tau)\mathrm{d}y_1 \tag{31}$$

and

$$\Pi_w(\overline{t}_r) = \sum_{k=1}^{N} 2\overline{\Gamma}_k\left(\sin\theta\frac{\partial}{\partial\overline{t}}\int_{-\infty}^{\overline{t}_r}\frac{\overline{V}_{\Gamma_k}^{(2)}\mathrm{d}\tau}{\sqrt{\overline{t}_r-\tau}} - \cos\theta\frac{\partial}{\partial\overline{t}}\int_{-\infty}^{\overline{t}_r}\mathrm{Re}\left\{\frac{\left(\overline{V}_{\Gamma_k}^{(1)} + i\overline{V}_{\Gamma_k}^{(2)}\right)\overline{z}_{\Gamma_k}\mathrm{d}\tau}{\sqrt{\left(\overline{t}_r-\tau\right)\left(\overline{z}_{\Gamma_k}^2-1\right)}}\right\}\right). \tag{32}$$

Late-time evaluation of $\Pi_{\xi_{\text{rigid}}}$ (cf. Eq. (26)) yields

$$\Pi_{\xi_{\text{rigid}}}(\bar{t}_r) \approx -\sqrt{\frac{2}{\pi}} \cos\theta\, \bar{\varepsilon}_h\, \bar{\omega}_h^{5/2} \cos\left(\bar{\omega}_h \bar{t}_r - \pi/4\right) \quad , \quad \bar{t}_r \gg \bar{\omega}_h^{-1}. \tag{33}$$

Results for the acoustic field are presented in terms of the acoustic "kernels" Π_{tot}, Π_ξ and Π_w. In addition to the non-dimensional parameters in Eq. (29), the acoustic pressure is also governed by the observer far-field directivity, $\theta = \cos^{-1}(x_2/|\mathbf{x}|)$. Since the "lift" ($\theta = 0$) dipole is considerably larger than the "suction" ($\theta = \pi/2$) component, we present our results in terms of the former only. Additionally, while the scheme of solution follows the system evolution since $\bar{t} = 0$ (when heaving actuation commences), we skip the description of the initial transient response, and focus on analyzing the system final periodic state.

3. Results

We start by examining the system behavior in the low stiffness limit of $\bar{R} \ll 1$. Towards this end, Fig. 2 examines the convergence of the far-field radiation of a highly-elastic filament ($\bar{R} \to 0$) to a membrane ($\bar{R} = 0$) system. Fig. 2a presents the variation with heaving frequency of the lift dipole amplitude for several values of $0 \le \bar{R} \le 10^{-1}$. Also presented are the frequency variations of the maximal structure deflection in Fig. 2b (obtained at the filament free end) and the amplitude of structure circulation (Fig. 2c), given by

$$\bar{\Gamma}_s(\bar{t}) = \int_{-1}^{1} \bar{\gamma}(\bar{x}_1, \bar{t}) \mathrm{d}\bar{x}_1. \tag{34}$$

In common to all figures, the effect of increasing $\bar{R}$ on the far- and near-field system behaviors is nearly indiscernible for $\bar{\omega}_h \lesssim 1$. Yet, for $\bar{\omega}_h \gtrsim 1$, all $\bar{R} \neq 0$ systems deviate from the membrane $\bar{R} = 0$ response, where the deviation occurs at lower $\bar{R}$ for higher $\bar{\omega}_h$. Convergence between the membrane and elastic-filament systems is therefore achieved at smaller actuation

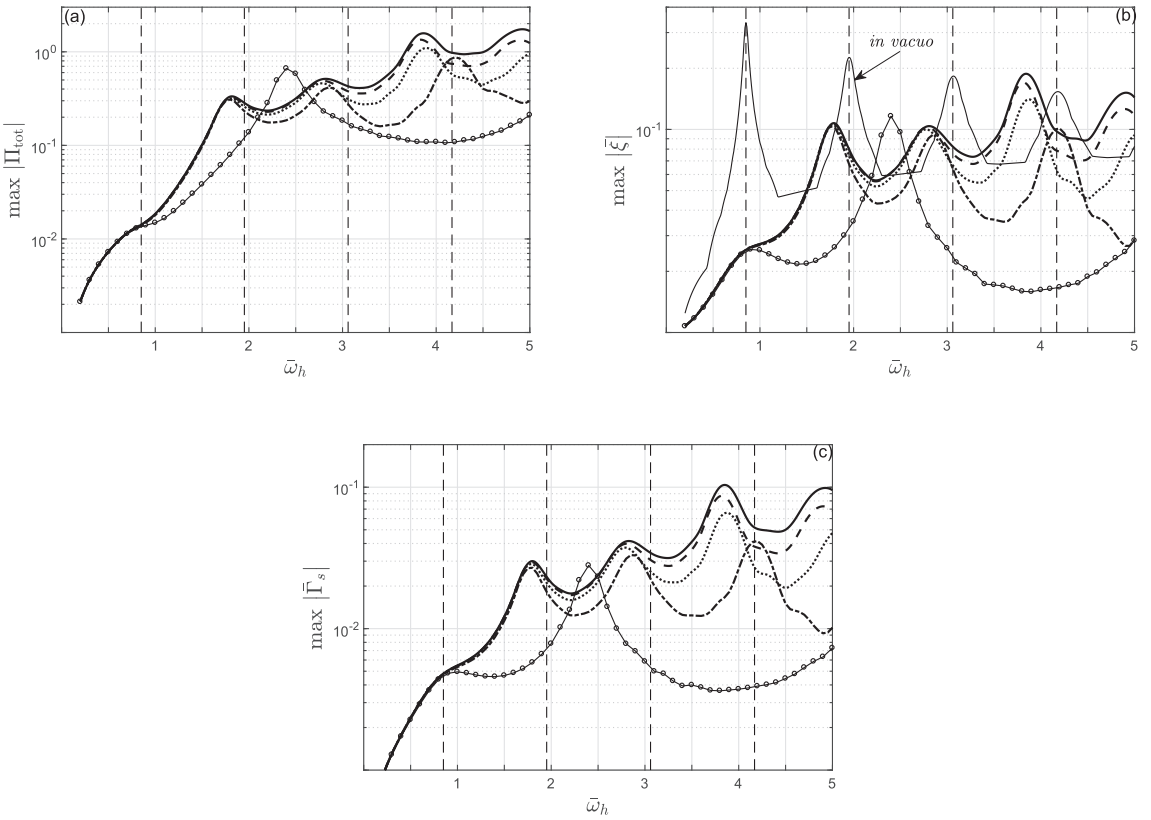

Fig. 2. Effect of actuation frequency on the system response at low rigidities: convergence of the filament to the membrane solution for $\bar{R} \to 0$. (a) Lift-dipole amplitude; (b) maximal filament deflection; (c) filament circulation amplitude. The results are presented for $\bar{R} = 0$ (solid line —), 10^{-5} (dashed line - - -), 10^{-4} (dotted line · · ·), 10^{-3} (dash-dotted line -·-·-), and 10^{-1} (solid circled line -o – o-). The dashed vertical lines denote the membrane ($\bar{R} = 0$) *in vacuo* eigenfrequencies, and the thin solid curve in Fig. 2b marks the membrane maximal deflection at *in vacuo* conditions.

frequencies for larger $\overline{R}$. Focusing on the system lift dipole in Fig. 2a, we also observe that, in general, the highest sound levels are generated by the membrane. Thus, when considering highly elastic configurations, bending stiffness tends to attenuate the sound level produced by the system. One exception is depicted by the $\overline{R}=10^{-1}$ curve, showing that the $\overline{R}=10^{-1}$ setup turns noisier than the membrane (and all other $\overline{R}\leq 10^{-1}$ systems) in the vicinity of $\overline{\omega}_h\approx 2.4$.

To rationalize this result, Fig. 2b and 2c presents the frequency variations of the maximal structure deflection and total circulation. The results support the above observation by showing an increase in the deflection and circulation amplitudes at $\overline{R}=10^{-1}$ and $\overline{\omega}_h\approx 2.4$, above the counterpart $\overline{R}=0$ values. At a fixed value of $\overline{R}$, Fig. 2b illustrates a resonance-like response of the system, where peak values are obtained at the system eigenfrequencies. This is reminiscent of the "hanging chain" *in vacuo* system response shown by the thin solid line [26]. Taking the membrane as a reference setup, any increase in $\overline{R}$ results in a shift in the system resonance frequencies to larger values. Thus, at a large enough value of the filament rigidity (as in the $\overline{R}=10^{-1}$ case), the shifted eigenfrequency occurs at a frequency that is far from the respective resonance of the membrane. It is therefore the accumulative change with $\overline{R}$ in the near-field fluid-structure interaction, reflected by the differences between systems eigenfrequencies and associated structures circulations, that results in increased noise levels of the elastic-body system.

The acoustic field of a highly elastic filament is further analyzed in Fig. 3a–d, focusing on the case of a membrane ($\overline{R}=0$), and presenting the effect of the actuation frequency on the total lift dipole Π_{tot}, together with its motion (Π_{ξ}) and wake (Π_w) components. The results are illustrated at the first four eigenfrequencies of the membrane, $\overline{\omega}_h\approx 0.8, 1.8, 2.8$ and 3.9, as depicted by the bold solid line in Fig. 2b. Keeping the same frequencies, Fig. 3e–h shows the instantaneous wake forms of the system, obtained at period time.

Starting with Fig. 3a–d, the results indicate that the wake dipole amplitude is larger than the motion dipole, and that the two contributions generally counteract. Consequently, the total signal levels in between the two components, and is slightly weaker than the wake dipole. The results further show that, while low-frequency ($\overline{\omega}_h\lesssim 1$) actuations result in a nearly harmonic signal (as in Fig. 3a), higher-frequency responses (as in Fig. 3b–d) are characterized by more complex waveforms. As illustrated by Fig. 3f–h, these are associated with increasingly irregular wake forms. Inspecting the motion and wake dipole components presented in Fig. 3b–d, we find that it is the motion dipole contribution, rather than the wake component, associated with a more complex flapping motion at increasing frequencies, that results in the non-harmonic form of the total signal.

To examine the effect of non-small filament rigidities on the system far-field response, Fig. 4 compares between the $\overline{\omega}_h$-variations of the motion (dashed line), wake (dash-dotted line) and total (solid curve) lift dipole amplitudes for $\overline{R}=0, 0.1, 2$ and 10^3. The dashed vertical lines mark the *in vacuo* eigenfrequencies at each $\overline{R}$. With increasing $\overline{R}$, the differences between consecutive eigenfrequencies increase, so that for the largest $\overline{R}=10^3$ presented (Fig. 4d), none of the *in vacuo* eigenvalues is contained within the $0<\overline{\omega}_h\leq 5$ interval.

The membrane system response, presented in Fig. 4a, reproduces the results in Fig. 3 for all frequencies considered, indicating that the wake sound dominates the motion contribution at all conditions. The total dipole amplitude then lies between the two components, showing that the motion and wake dipoles essentially counteract. Increasing the filament rigidity to $\overline{R}=0.1$ (Fig. 4b), we find that, while the wake dipole remains the dominant source of sound at most frequencies, the motion dipole becomes of similar amplitude in the vicinity of the second filament eigenfrequency, as well as towards the third eigenfrequency (not presented here). Increasing $\overline{R}$ further in Fig. 4c and 4d, the results indicate a threshold frequency ($\overline{\omega}_h\approx 2.6$ for $\overline{R}=2$; $\overline{\omega}_h\approx 1.2$ for $\overline{R}=10^3$), above which the motion dipole becomes dominant. Notably, for $\overline{R}=10^3$, the filament motion dipole coincides with its rigid-body counterpart in Eq. (33), shown by the dashed line in Fig. 4d. At this value of $\overline{R}$ and the interval of frequencies considered, the filament may therefore be treated as a rigid body. Since the motion dipole increases as $O(\overline{\omega}_h^{5/2})$, it practically becomes the sole source of sound at large enough frequencies. This is illustrated by the convergence of the $\left|\Pi_{\xi}\right|$ curve to the $\left|\Pi_{\text{tot}}\right|$ line in Fig. 4d for $\overline{\omega}_h\gtrsim 3$.

Reviewing the results in Fig. 4, we find that the acoustic signal is dominated by the wake contribution at low enough actuation frequencies for all $\overline{R}$. With increasing $\overline{R}$ and at non small frequencies, the motion dipole overcomes the wake contribution. When considering large enough $\overline{R}$, the system captures its rigid-body signature within an increasingly wider interval of frequencies. The extent of the $\overline{\omega}_h$ interval through which the system acquires a rigid body response may be assessed by comparing between the solid lines in Fig. 4a–d. Thus, taking the solid line in Fig. 4d for $\overline{R}=10^3$ as the reference "rigid-body signature", we observe that the solid lines in Fig. 4a–c are nearly identical at low enough $\overline{\omega}_h<1$. With increasing $\overline{\omega}_h$, these curves deviate from the rigid-body result at increasingly larger $\overline{\omega}_h$ for larger $\overline{R}$. This deviation reflects the effect of system elasticity on the system signature, realized by the non-trivial flapping motion and associated wake dynamics (see Fig. 3e–h).

To fully illustrate the system transition between its "rigid" and "non-rigid" fluid-structure interaction characteristics, Fig. 5a presents the variations with $\overline{R}$ of the lift dipole amplitude at discrete values of $\overline{\omega}_h$. Here the dashed horizontal lines mark the membrane and rigid-body limit values. Fig. 5b shows the variation with $\overline{\omega}_h$ of the phase difference $\overline{\varphi}$ between the motion and wake lift dipoles at the indicated values of $\overline{R}$. The phase difference is defined by the radian difference between the occurrences of $\max\left|\Pi_{\xi}\right|$ and $\max\left|\Pi_w\right|$ along a period. The values of $\overline{\varphi}=0, 2\pi$ correspond to in-phase signals, whereas $\overline{\varphi}=\pi$ denotes counter-phase signals.

Starting with low-frequency actuations, both figures support the previous observation that for small enough $\overline{\omega}_h$ the structure deflects as a rigid body. This can be viewed by the exceedingly small $\overline{R}$-variations in the $\overline{\omega}_h=0.5$ curve in Fig. 5a, as well as by

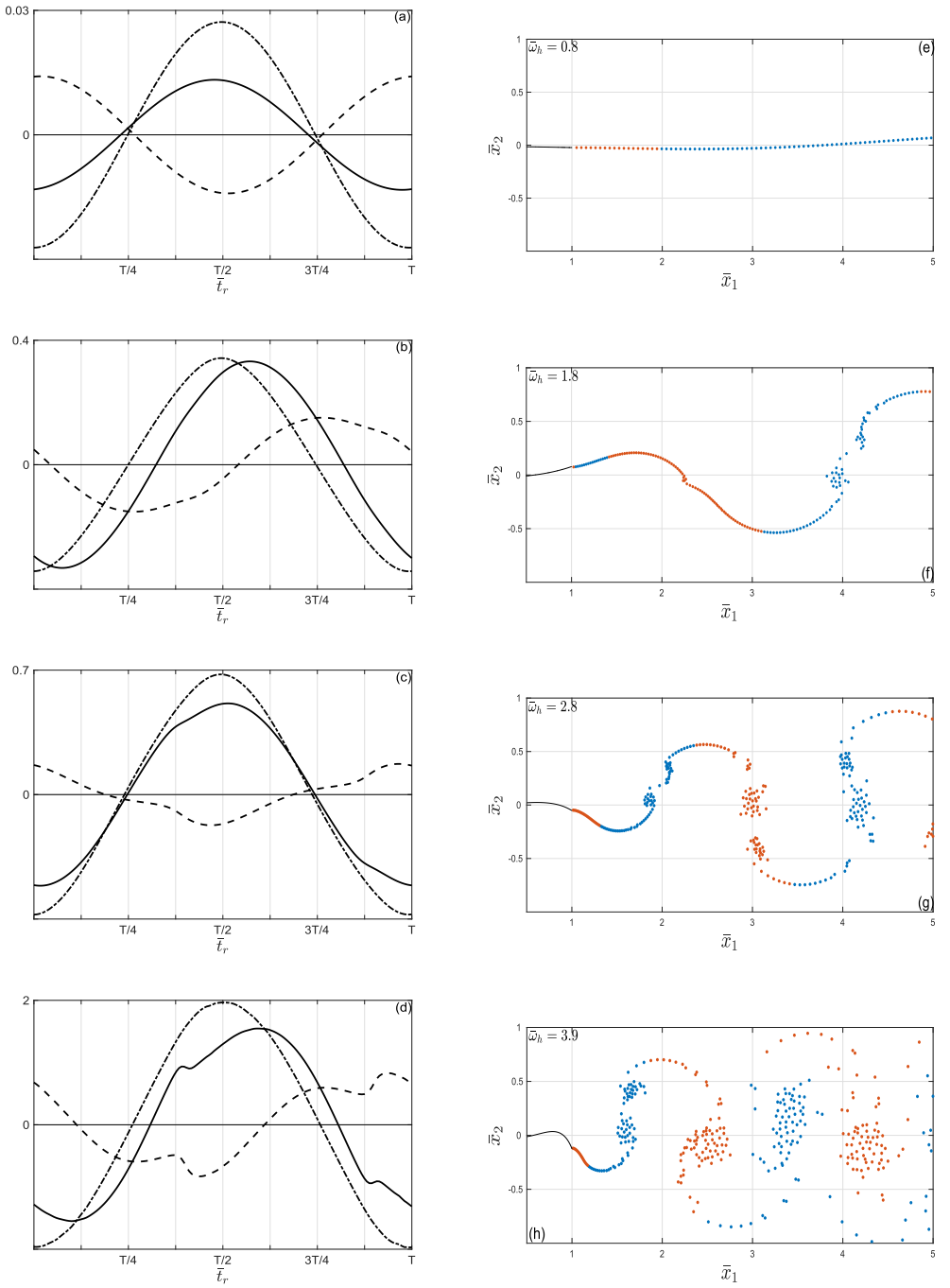

Fig. 3. Effect of actuation frequency on the membrane ($\overline{R} = 0$) response: far field radiation and wake dynamics. (a–d) Period time variations of the total lift dipole and its components for $\overline{\omega}_h = 0.8$ (a), 1.8 (b), 2.8 (c), and 3.9 (d). The solid (—), dashed (- - -) and dash-dotted (-·-·-) curves mark the total (Π_{tot}), motion (Π_s), and wake (Π_w) lift dipoles, respectively. (e–h) Instantaneous wake forms at period time. The blue and red dots mark vortices with counterclockwise and clockwise vorticities, respectively. The solid lines show the instantaneous filament shapes. (For interpretation of the references to colour in this figure legend, the reader is referred to the Web version of this article.)

the convergence of all curves in Fig. 5b to a single phase at low $\overline{\omega}_h$. With increasing frequency, however, filament elasticity turns significant, and affects the system acoustic signal. Thus, for $\overline{\omega}_h \gtrsim 1$, the total sound amplitude exhibits local and global extrema at intermediate values of $\overline{R}$ between the membrane and rigid plate limits. The global maxima reflects the natural frequency response of the configuration – where, for example, the maximum point in the $\overline{\omega}_h = 2.4$ curve at $\overline{R} = 10^{-1}$ occurs at the configuration second eigenfrequency, depicted by the solid circled line in Fig. 2b. To rationalize the global minima, the phase

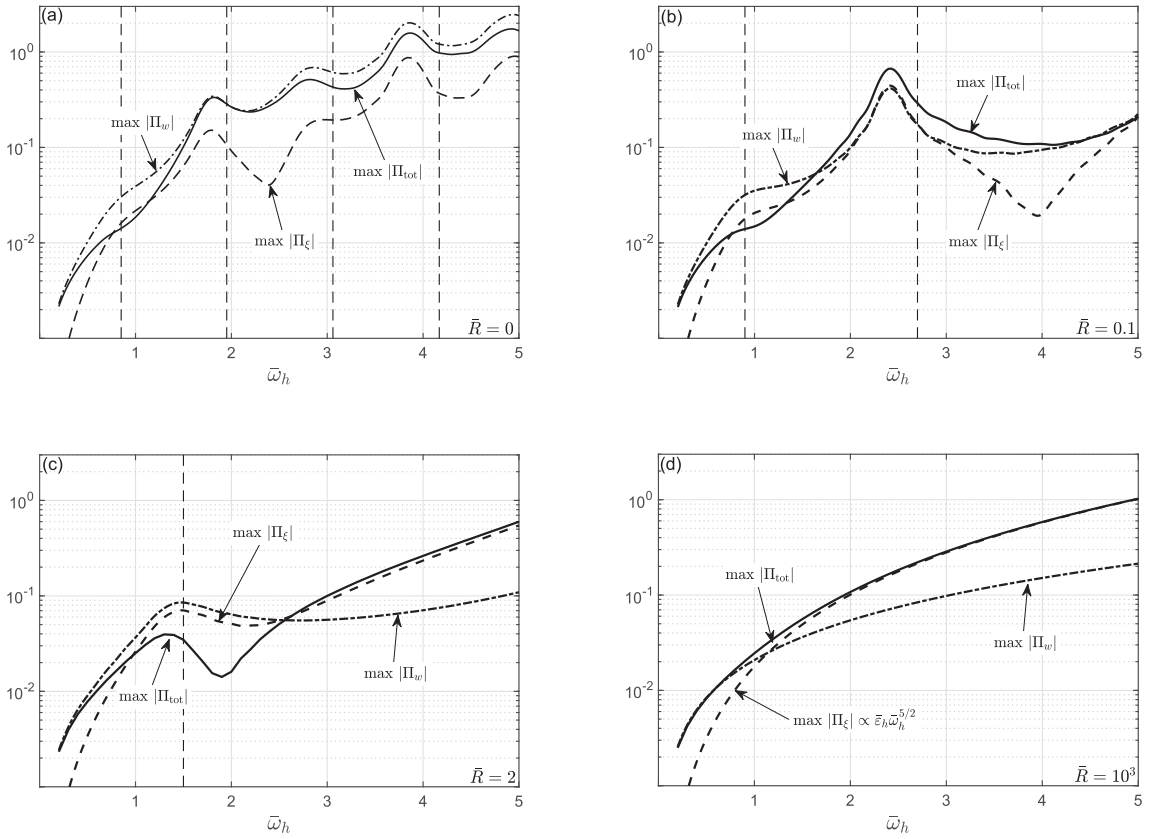

Fig. 4. Effects of flexural stiffness and actuation frequency on the system far field response: variations with $\overline{\omega}_h$ of the acoustic signal amplitudes at $\overline{R}=0$ (a), $\overline{R}=0.1$ (b), $\overline{R}=2$ (c), and $\overline{R}=10^3$ (d). The solid (—), dashed (- - -) and dash-dotted (-·-·-) curves mark the amplitudes of the total lift dipole ($\Pi_{\rm tot}$), and the corresponding motion (Π_ξ) and wake (Π_w) components, respectively. The dashed vertical lines denote the filament *in vacuo* eigenfrequencies at each value of $\overline{R}$.

difference between the motion and wake dipole components should be considered. Inspecting Fig. 5b, we find that the sharp minimum obtained in Fig. 5a for $\overline{\omega}_h=1.8$ at $\overline{R}=2$ occurs where the two components are opposite in phase (see the point where the solid-squared line crosses $\overline{\varphi}=\pi$ in Fig. 5b). As observed in Fig. 4c, at this combination of $\overline{R}=2$ and $\overline{\omega}_h=1.8$, the motion and wake components are of similar amplitude, thus resulting in a nearly optimal cancellation effect. In a similar manner, the global minima observed in Fig. 5a for $\overline{\omega}_h\approx 2.4, 3$ and 4 follow from comparable magnitude and counter-phased motion and wake dipoles, crossing $\overline{\varphi}\approx\pi$ at the respective $(\overline{R},\overline{\omega}_h)$ combinations in Fig. 5b.

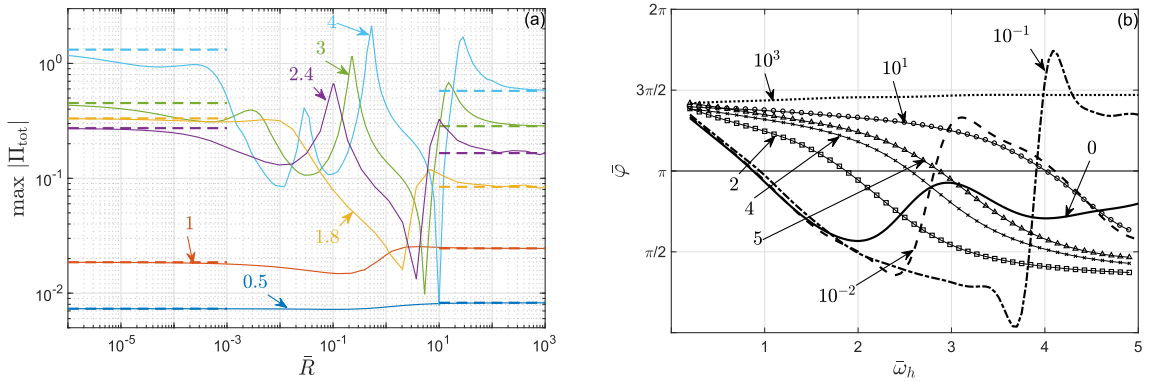

Fig. 5. Effects of flexural stiffness and actuation frequency on the system far-field response: (a) Variation with $\overline{R}$ of the lift dipole amplitude at the indicated values of $\overline{\omega}_h$. (b) Variation with $\overline{\omega}_h$ of the phase difference $\overline{\varphi}$ between the motion and wake lift dipoles at the indicated values of $\overline{R}$. The values $\overline{\varphi}=0, 2\pi$ correspond to in-phase acting signals, while $\overline{\varphi}=\pi$ denotes counter-phase signals. In Fig. 5a, the left and right dashed lines (- - -) mark the membrane and rigid-body limit values at each $\overline{\omega}_h$, respectively.

With increasing actuation frequency, the "counter-phase state" where $\overline{\varphi} = \pi$ occurs at higher values of $\overline{R}$. Consequently, the filament convergence to a rigid-body type of motion is obtained at higher rigidities (cf. the convergence of the different curves in Fig. 5a to their rigid-body limits). The occurrence of a "counter-phase frequency" is not encountered in a rigid filament setup (with $\overline{R} \gtrsim 10^3$), where the phase difference remains nearly unchanged ($\overline{\varphi} \approx 3\pi/2$ for all $\overline{\omega}_h$ considered). It is therefore the combined effects of intermediate values of $\overline{R}$ and $\overline{\omega}_h$ that result in the above-described mechanism of sound cancellation, which may prove useful as a means for flapping-motion sound reduction.

4. Conclusion

We studied the acoustic far field of a thin flexible filament subject to uniform mean flow and a 'hanging chain' external force parallel to its unperturbed state. The filament was harmonically actuated at its upstream edge with small-amplitude heaving motion and prescribed frequency. By varying the filament flexural rigidity, we analyzed the system far field radiation for all stiffnesses, ranging from a membrane to a rigid body. Assuming two-dimensional high Reynolds and low Mach number flow, a near-field description was applied based on potential thin airfoil theory and a discrete wake model, to formulate the source term in the Powell-Howe acoustic analogy. The far field sound was then calculated using a compact Green's function approach, yielding the leading order acoustic dipole field. In the limit of small flexural stiffnesses, we found that the acoustic field of a highly-elastic filament converges to the far field of a hanging membrane, both dominated by the wake dipole sound. The wake sound contribution also dominates in the limit of small actuation frequencies, where the filament deflects as a rigid body regardless of its structural stiffness. Sufficient increase in heaving frequency then amplifies the relative contribution of filament motion dipole, resulting in significant differences between systems with different rigidities. Reflecting the impact of filament elasticity, these differences manifest the system's natural frequency response, leading to increased levels of sound for actuations at one of the system's eigenfrequencies. In cases where the trailing edge wake and motion dipoles acquire similar amplitudes and opposite phases, significant sound reduction was found. With increasing frequency, rigid-body filament motion and far-field signature were captured above increasingly higher values of the body structural rigidity.

The study has focused on the case of harmonic excitation, and analyzed the effects of actuation frequency and body bending stiffness on the system response. In applications where the body stiffness is fixed, the present framework may still be useful for analyzing the far-field fluid response to arbitrary (small-amplitude, even if broadband) filament actuation, as well as to other forms of external loading (e.g., incoming flow non-uniformity). In this respect, considering our investigation as a generalized Fourier analysis, it is expected that any external excitation, when discretized into its spectral components, should reflect the system modal response as obtained by the current calculation. Additional topics, such as the near- and far-field investigations of the unforced (critical and supercritical) system response, are subjects for future studies.

Appendix A. Supplementary data

Supplementary data related to this article can be found at https://doi.org/10.1016/j.jsv.2018.07.014.

References

[1] M.S. Howe, Acoustics of Fluid-structure Interactions, Cambridge University Press, Cambridge, UK, 1998.
[2] L. Huang, Mechanical modeling of palatal snoring, J. Acoust. Soc. Am. 97 (1995) 3642–3648.
[3] H.C. Bennet-Clark, Acoustics of insect song, Nature 234 (1971) 255–259.
[4] S. Drosopoulos, M.F. Claridge, Insect Sounds and Communication: Physiology, Behaviour, Ecology and Evolution, Taylor and Francis, Boca Raton, Florida, 2006.
[5] R.R. Graham, The silent flight of owls, J. R. Aeronaut. Soc. 286 (1934) 837–843.
[6] K. Chen, Q. Liu, G. Liao, Y. Yang, L. Ren, H. Yang, X. Chen, The sound suppression characteristics of wing feather of owl (bubo bubo), JBE 9 (2012) 192–199.
[7] T.F. Brooks, D.S. Pope, M.A. Marcolini, Airfoil Self-noise and Prediction, vol. 1218, National Aeronautics and Space Administration, Office of Management, Scientific and Technical Information Division, 1989.
[8] O. Zaporozhets, V. Tokarev, K. Attenborough, Aircraft Noise, Taylor and Francis, New York, 2011.
[9] S. Alben, M.J. Shelley, Flapping states of a flag in an inviscid fluid: bistability and the transition to chaos, Phys. Rev. Lett. 100 (2008) 074301.
[10] M.J. Shelley, J. Zhang, Flapping and bending bodies interacting with fluid flows, Annu. Rev. Fluid Mech. 43 (2011) 449–465.
[11] J.J. Allen, A.J. Smits, Energy harvesting eel, J. Fluid Struct. 15 (2001) 629–640.
[12] J.C. Liao, D.N. Beal, G.V. Lauder, M.S. Triantafyllou, Fish exploiting vortices decrease muscle activity, Science 302 (2003) 1566–1569.
[13] S. Michelin, S.G. Llewellyn Smith, Resonance and propulsion performance of a heaving flexible wing, Phys. Fluids 21 (2009) 071902.
[14] A. Manela, Vibration and sound of an elastic wing actuated at its leading edge, J. Sound Vib. 331 (2012) 638–650.
[15] A. Manela, On the acoustic radiation of a pitching airfoil, Phys. Fluids 25 (2013) 071906.
[16] S. Alben, Optimal flexibility of a flapping appendage in an inviscid fluid, J. Fluid Mech. 614 (2008) 355–380.
[17] A. Manela, M.S. Howe, The forced motion of a flag, J. Fluid Mech. 635 (2009) 439–454.
[18] S.K. Datta, W.G. Gottenberg, Instability of an elastic strip hanging in an airstream, J. Appl. Mech. 42 (1975) 195–198.
[19] C. Lemaitre, P. Hemon, E. de Langre, Instability of a long ribbon hanging in axial air flow, J. Fluid Struct. 20 (2005) 913–925.
[20] C. Grouchier, S. Michelin, R. Bourget, Y. Madarres-Sadeghi, E. de Langre, On the efficiency of energy harvesting using vortex-induced vibrations of cables, J. Fluid Struct. 49 (2014) 427–440.
[21] G. Frey, B. Carmichael, J. Kavanaugh, S.N. Mahmoodi, Dynamic model and simulation of flag vibrations modeled as a membrane, in: Proceedings of the ASME 2014 Dynamics Systems and Control Conference, San Antonio, TX, 2014, DSCC2014–5897.
[22] G. Frey, S.N. Mahmoodi, Forced response analysis of a piezoelectric flag modeled as a membrane, in: Proceedings of the ASME 2015 Smart Materials, Adaptive Systems, and Intelligent Structures Conference, Colorado Springs, CO, USA, 2015, SMASIS2015–9013.
[23] G. Frey, Modeling a Piezoelectric Flag as a Membrane for Energy Harvesting, MSc Thesis, The University of Alabama, 2015.
[24] A. Manela, M. Weidenfeld, The 'hanging flag' problem: on the heaving motion of a thin filament in the limit of small flexural stiffness, J. Fluid Mech. 829 (2017) 190–213.

[25] E. Pedersen, F. Berg, R. Bakker, J. Bouma, Response to noise from modern wind farms in The Netherlands, J. Acoust. Soc. Am. 126 (2009) 634–643.
[26] P. Hagedorn, A. Dasgupta, Vibrations and Waves in Continuous Mechanical Systems, Wiley, Chichester, England, 2007.
[27] A. Purohit, A.K. Darpe, S.P. Singh, Experimental investigations on flow induced vibration of an externally excited flexible plate, J. Sound Vib. 371 (2016) 237–251.
[28] M. Weidenfeld, A. Manela, On the attenuating effect of permeability on the low frequency sound of an airfoil, J. Sound Vib. 375 (2016) 275–288.
[29] M.S. Howe, Theory of Vortex Sound, Cambridge University Press, Cambridge, 2003.
[30] A. Manela, Nonlinear effects of flow unsteadiness on the acoustic radiation of a heaving airfoil, J. Sound Vib. 332 (2013) 7076–7088.